Elastic interfacial layer enabled the high-temperature performance of lithium-ion batteries via utilization of synthetic fluorosulfate additive

Nam-Soon Choi (nschoi@kaist.ac.kr)
Korea Advanced Institute of Science and Technology https://orcid.org/0000-0003-1183-5735
Hyeongyu Moon
Korea Advanced Institute of Science and Technology
Huibeom Nam
Hyundai Motor Company
Min Pyeong Kim
Ulsan National Institute of Science and Technology
Seung Min Lee
Ulsan National Institute of Science and Technology
Hyeongjun Kim
Ulsan National Institute of Science and Technology
Min Ho Jeon
Ulsan National Institute of Science and Technology
Yoon-Sung Lee
Hyundai Motor Company
Koeun Kim
Hyundai Motor Company
Joong-Hyun Chun
Yonsei University College of Medicine
Sang Kyu Kwak
Ulsan National Institute of Science and Technology https://orcid.org/0000-0002-0332-1534
Sung You Hong
Ulsan National Institute of Science and Technology https://orcid.org/0000-0002-5785-4475

Article

Keywords:

Posted Date: July 27th, 2022

DOI: https://doi.org/10.21203/rs.3.rs-1823759/v1

Abstract

Ensuring interfacial stability of Si-containing anodes and Ni-rich cathodes is the key to achieving high-energy lithium-ion cells. Herein, we present 4-(allyloxy)phenyl fluorosulfate (APFS), a multi-functional electrolyte additive that forms a mechanical strain-adaptive solid electrolyte interphase (SEI) composed of LiF and polymeric species, and a thermally stable cathode–electrolyte interface containing S–O and S–F species. Radical copolymerization of vinylene carbonate (VC) with APFS via electrochemical initiation creates a spatially deformable polymeric SEI on the Si/C-graphite (SiG-C) anode with large volume changes during cycling. Here we show that APFS-promoted interfacial layers reduce Ni dissolution and deposition and that APFS deactivates Lewis acidic PF_5, inhibiting the hydrolysis that produces unwanted HF. These results show that the combined use of VC and APFS allows capacity retention of 72.5% with a high capacity of 143.5 mAh g^{-1} after 300 cycles at 45°C.

Introduction

High-energy lithium-ion batteries (LIBs) are critical for powering electric vehicles (EVs)[1–5]. Building EV-adaptable batteries that cover 500 km on a single charge requires high-capacity Si-containing anode materials and high-Ni layered oxide cathodes having a high reversible capacity of over 200 mAh g^{-1}. However, large volume fluctuation of silicon induced by repeated alloying and dealloying processes and structural instability of high-Ni $LiNi_xCo_yMn_{1-x-y}O_2$ (NCM) cathodes through an irreversible phase transition and micro-cracking make the practical application difficult[6–11]. Fluoroethylene carbonate (FEC) promoted-solid electrolyte interphase (SEI) can improve the electrochemical reversibility of silicon-containing anodes. However, the insufficient chemical stability of FEC in $LiPF_6$-incorporated electrolytes does not assure the long-term cycle performance of LIBs, particularly at elevated temperatures[12]. Dehydrofluorination of FEC caused by Lewis acidic PF_5 generates corrosive hydrofluoric acid (HF), which may impair cell performance due to structural and compositional damage to the electrolyte–electrode interfaces. In addition, vinylene carbonate (VC) along with FEC, has been frequently employed as a reductive additive to form SEI on the Si anode[13–15]. However, densely spaced poly(VC)-based SEI cannot retain large spatial volume fluctuation of Si during alloying and dealloying processes with Li. Thus, developing synthetic electrolyte additives that can overcome the limitations of VC and FEC is critically important[16–22].

The deterioration of the electrochemical performance of high-Ni NCM cathodes is mostly due to severe degradation of the interfacial structure. Cathode–electrolyte interface (CEI)-forming additives that contain heteroatoms have been the subject of many studies concerning high-Ni NCM cathode. The addition of 1,3-propane sultone (PS) and VC significantly improved the high-temperature performance of $LiNi_{1/3}Co_{1/3}Mn_{1/3}O_2$ (NCM111)/graphite full cells[23,24]. In addition, sulfur-containing additives, such as 1,3,2-dixathiolane-2,2-dioxide (DTD) and 4-propyl-[1, 3, 2]dioxathiolane-2,2-dioxide (PDTD), were introduced to construct a thermally robust lithium alkyl sulfonate-based CEI and stabilize high-Ni layered oxides[25,26]. In addition, boron-centered lithium bis(oxalate)borate (LiBOB) has been presented to enhance

the electrochemical behaviors of NCM111/mesocarbon microbeads full cells at elevated temperatures and increase the thermal stability of the 4.3 V-charged NCM111 cathodes[27]. This is attributed to the ability of electron-deficient boron atom in the LiBOB-derived CEI to stabilize PF_5, which is a reactive substance that would otherwise produce unwanted HF in $LiPF_6$-based electrolyte[28]. Although PS is effective for forming thermally stable SEI with inorganic species such as Li_2SO_3 on graphite anodes, its suitability for Si-containing anodes and high-Ni NCM cathodes has not been verified. Moreover, LiBOB is less likely to form LiF-rich SEI, which can accommodate mechanical stress induced by the lithiation of Si. Therefore, developing electrolyte additives that create appropriate interfacial layers for high-Ni NCM cathodes and Si-containing anodes is essential to adjust the performance of batteries powering EVs.

In this study, we describe the incorporation of a functional fluorosulfate-based additive, 4-(allyloxy)phenyl fluorosulfate (APFS), to create elastic and thermally stable interfacial layers on electrodes and enhance the electrochemical property of SiG-C/$LiNi_xCo_yMn_{1-x-y}O_2$ (NCM811) full cells. Cycling studies in cells reveal that using APFS in the VC-added electrolytes enables stable operation of a 20.5 mAh cm^{-2} high-mass-loaded SiG-C/NCM811 full cell. Moreover, spectral studies reveal that the combined formulation of VC and APFS allows tuned deformability of SEI suitable for SiG-C anodes and enhanced inhibition toward the structural degradation and Ni ion loss of the NCM811 cathode.

Results

The multi-property-inspired concept for the APFS structure is shown in Fig. 1a. The APFS bearing the vinyl and fluorosulfate groups as a functional electrolyte additive was synthesized through successive allylation, sulfurylation, and fluorination. The detailed synthetic procedures and nuclear magnetic resonance (NMR) data are illustrated in Fig. 1b and Supplementary Fig. 1[29].

Cycle performance of SiG-C/NCM811 full cells. The orbital energy levels highest occupied molecular orbital (HOMO) and lowest unoccupied molecular orbital (LUMO)) of solvents and additives were theoretically compared. The APFS additive exhibited the lowest LUMO energy level of − 1.009 eV and the highest HOMO energy level of − 6.780 eV, implying a better tendency for reductive and oxidative decomposition than others at the SiG-C anode and NCM811 cathode, respectively (Fig. 1c). Furthermore, the deformation energy of APFS during its reduction is relatively lower than that of other components (Fig. 1d), indicating the favorable decomposition of reduced APFS. In addition, the F dissociation energies, which is the amount of energy required to detach a fluorine atom from an additive, of all components are compared. APFS is expected to be a more effective source of LiF[30] than FEC because its F dissociation energy is lower than that of FEC, which is supported theoretically. (Fig. 1e). LiF in SEI is an effective component which can ensure the interfacial stability of silicon-containing anodes, which suffer from volume changes during cycling. In addition, LiF can favorably bind with Li ions of the organic-rich SEI components and lithiated anodes[31].

Figure 2a–e show the cycle performance of SiG-C/NCM811 full cells with 1 wt% VC-, 1 wt% VC + 2 wt% FEC-, and 1 wt% VC + 0.5 wt% APFS- incorporating electrolytes at 45 °C and 1 C rate under the electrolyte mass to cell capacity (E/C) ratio of 5.6 mg mAh^{-1}. The VC-containing electrolyte showed severe capacity decay after 50 cycles and inferior capacity retention of 33.2% while delivering a discharge capacity of 65.2 mAh g^{-1} after 300 cycles at 45 °C (Fig. 2a). Conversely, VC + APFS-containing electrolyte exhibited significantly improved capacity retention of 72.5% and presented a discharge capacity of 143.5 mAh g^{-1}, which was slightly better than that of the VC + FEC-containing cells. Furthermore, the Coulombic efficiency of VC + FEC reached 99.5% after 50 cycles, whereas that of VC + APFS quickly reached 99.5% within 10 cycles (Fig. 2b–e). As shown in Supplementary Fig. 2, the optimal content of 0.5 wt% APFS is required to ensure the optimal interfacial stability of the electrodes and mitigate the harmful impacts of reactive species, such as PF_5 generated from $LiPF_6$-based electrolytes. APFS decomposes reductively at 1.1 V vs. Li/Li^+ during the initial cathodic scan (lithiation) of the anode. Moreover, the VC reduction peak disappeared for the VC + APFS electrolyte, indicating the co-decomposition of APFS and VC (Fig. 2f). The VC + APFS electrolyte effectively mitigated the undesired decomposition reactions of electrolytes at electrodes leading to capacity loss and drastically enhanced the cycle stability of SiG-C/NCM811 full cells at 25 °C and 1 C (Fig. 2g–j). A cell with VC + APFS enhanced the fast-charge performance of SiG-C/NCM811 full cells at charge rates of 2 C and 3 C compared with a VC-containing cell at 25 °C (Fig. 2k). The interfacial impedance (surface film resistance + charge-transfer resistance) was decreased from 33.6 Ω to 25.4 Ω by using VC + APFS (Fig. 2l).

APFS-derived SEI on SiG-C anode. The beneficial role of the VC + APFS electrolyte in the SEI structure of the SiG-C anode was examined through an ex-situ X-ray photoelectron spectroscopy (XPS) study. As APFS has a relatively low LUMO energy level, it is expected to undergo electrochemical reduction at the SiG-C anode preferentially. The decomposition of APFS began at 2.7 V, while producing pronounced peaks attributed to the sulfur-based species (Fig. 3a). In the case of the VC + APFS electrolyte, a relatively strong LiF signal was detected for the anode compared to the VC-containing electrolyte (Fig. 3b and c). From this result, we surmised that the reduction of APFS cause LiF formation. The fluorosulfonyl functional group may release fluorine anion to form LiF, and the detachment of the SO_2F group from the APFS structure may lead to the sulfur-rich SEI formation. The peaks corresponding to SO_4^{2-}/SO_2F^- and SO_3^- moieties induced by the APFS reduction at the SiG-C anode appeared at 169.8 eV and 168.0 eV, respectively (Fig. 3c)[32]. In contrast to VC-derived SEI, which is made up of poly(VC)-containing inner SEI and P–F/LiF-rich outer SEI, VC + APFS comprises an organic-rich inner layer containing polymer species, a sulfur-rich middle layer, and a mechanically robust LiF-based outer SEI. Moreover, the C 1s XPS profiles of SiG-C anode confirmed the disparity in the reductive decomposition of VC and VC + APFS (Supplementary Fig. 3). Both electrolytes showed the formation of poly(VC) species at 3.0 V. Because of the copolymerization of VC and APFS at the SiG-C anode, VC-derived SEI was found to be primarily composed of poly(VC) species, whereas VC + APFS-derived SEI had a lower proportion of poly(VC). The relatively strong C–C signal corresponding to graphite indicates that VC + APFS creates a thin SEI compared to the VC-derived SEI, and a facile Li-ion transport is expected.

The expected reaction mechanisms for the formation of each inorganic and organic SEI, represented as path I and path II, respectively, are shown in Fig. 4. The reaction mechanisms were investigated via density functional theory (DFT) calculations to elucidate the contribution of each functional moiety of APFS on the build-up of the SEIs. Based on the low F dissociation energy (Fig. 1e), the direct formation of LiF is expected for path I. Furthermore, the one-electron reduction on APFS initiates another pathway of LiF formation, resulting in the breakage of the S–O bond at the core of the APFS and decomposition into SO_2F and APE–O groups (Supplementary Fig. 4). The distributed charge of each group was − 0.988 *e* and − 0.012 *e* in the SO_2F and APE–O groups, respectively. Therefore, we speculate an electron is mainly assigned to the SO_2F group, which leads to the formation of a SO_2F^- anion and an APE–O radical. Subsequently, the SO_2F^- anion is expected to contribute to the LiF formation by interacting with the Li^+ ion. With the most stable structure of Li^+–SO_2F^- ionic complex obtained by comparing the relative energies according to the various adsorption sites of Li^+ ion on the SO_2F^- anion (Supplementary Fig. 5), the energy diagram of the SO_2F^- anion decomposition was traced (Supplementary Fig. 6). The energy barrier and heat of reaction are thermodynamically favored with the presence of the Li^+ ion. As SO_2 has a much lower LUMO level (− 3.67 eV) than APFS (− 1.01 eV), SO_2F^- anion (0.53 eV), and LiF (0.61 eV) (Supplementary Fig. 7), it is more favorable to accept an electron to form the SO_2^- anion[22]. In contrast, for path II, the APE–O radical is expected to contribute to the copolymerization of VC and APFS. First, the polymerization may unfavorably proceed through the direct reaction of the APE–O radical with the sp^2 carbon in the vinyl group of VC and APFS, as shown by the considerably generated endothermicity (0.29 to 0.47 eV) (Supplementary Fig. 8). In contrast, the APE–O radical (*O*-centered) leads to the formation of an APFS radical (*C*-centered) through hydrogen atom transfer (HAT) reaction[33].Thus, the HAT reaction mechanisms of the APE–O radical with carbonate solvent molecules, VC, and APFS were investigated, and the hydrogen sites of the most favorable pathway were sought among the possible HAT reaction pathways (Supplementary Fig. 9). The reaction with APFS, where relative energies for each hydrogen site were checked (Supplementary Fig. 10), showed the lowest energy barrier (0.01 eV) and heat of reaction (0.07 eV). Hence, the APE–O radical was more likely to react with APFS, which became the APFS radical. Remarkably, the APFS radical could lead to the propagation step of radical copolymerization of VC and APFS (Supplementary Fig. 11). The reactions of the APFS radical with VC and APFS showed an energy barrier of 0.60 eV and 0.59 eV and a heat of reaction of − 0.02 eV and − 0.20 eV, respectively, indicating the plausible occurrence of reaction by exothermicity and low energy barrier[34]. Notably, successive reactions with VC and APFS were shown to be possible with low activation energy (0.18 to 0.30 eV) and exothermic heat of reaction (− 0.98 to − 0.67 eV) (Supplementary Fig. 12).

To this end, it is theoretically shown that the reductive decomposition of APFS contributes to the build-up of the inorganic outer SEI based on LiF and the organic inner SEI based on the radical copolymerization of VC and APFS on the SiG-C anode. It is thought that this SEI structure based on the inorganic outer SEI and organic inner SEI is effective for enhancing the cycle stability of SiG-C/NCM811 full cells. The amount of APFS in the electrolyte solution and SEI structure was explored through ^1H NMR and Fourier-

transform infrared (FT-IR) analyses to probe the contribution of the APFS additive to the SEI creation on the anode. ^{1}H NMR spectra (400 MHz, tetrahydrofuran (THF)-d_8) showed the decrease of characteristic resonances of the vinyl (C = C) group at a chemical shift of approximately 6.1 ppm and the phenyl ring at a chemical shift of approximately 7.1 ppm during charging, indicating both moieties of APFS are consumed to form the SEI (Fig. 5a). The decreased C = C peak intensity is in line with the polymeric SEI formation on the SiG-C anode showing the consumption of vinyl moieties within the APFS structure through the radical copolymerization between VC and APFS (Fig. 4). The reductive decomposition of the APFS additive is evident from the phenyl structure present in the SEI, as illustrated in Fig. 5b. Furthermore, an increased C–C stretch in the aromatic ring, C–H, C = C, and CH_2 signals in the vinyl group observed in the FT-IR spectra of the SiG-C anode with VC + APFS electrolyte indicate that the APFS additive undergoes reductive decomposition at the anode and contributes to the SEI formation. Figure 5c shows the proposed polymeric structures produced by the electrochemical reduction of VC and VC + APFS electrolytes. Phenyl moieties bonded to the poly(VC) backbone may hamper the tight packing of poly(VC) chains, leading to a dense and rigid SEI structure. C–O–C groups existing in the side chain of the polymer backbone formed by the copolymerization of VC and APFS can make the SEI possess more free-volume through their conformational rotation[35]. Owing to the reduced rigidity of the SEI, the VC + APFS-promoted SEI may have a high adsorption ability toward volumetric expansion of Si/C particles of the SiG-C anode. The mechanical properties of VC- and VC + APFS-derived SEI layers were investigated with contact mode atomic force microscopy (AFM) (Supplementary Fig. 13). Figure 5d shows that Young's modulus of the VC-containing anode substantially increased. The increased modulus may be attributable to the high infiltration level of pulverized Si/C particles into the SEI during cycling. This is probably because the VC-derived rigid and dense SEI does not endure large volumetric stress of Si/C particles and is physically damaged, increasing SEI thickness by continuous electrolyte decomposition and electrical isolation of cracked Si/C particles. In contrast, the anode with VC + APFS electrolyte had low values compared to the VC electrolyte, and no drastic increment was observed in Young's modulus. Low Young's modulus indicates high elasticity of the SEI[36]. It is clear that the more elastic VC + APFS-derived SEI adopts mechanical stress caused by the lithiation of the SiG-C anode and mitigates pulverization and electrical isolation of Si/C materials. Comparative scanning electron microscopy (SEM) studies on SiG-C anodes with VC, VC + FEC, and VC + APFS electrolytes after 100 cycles at 45°C revealed that a lower volume expansion of 109.5% was obtained for the cycled SiG-C anode with VC + APFS electrolyte than for those with VC (113.5%) and VC + FEC electrolyte (112.0%). This result can be attributed to the combined use of VC and APFS additives manipulating the interface structure of the SiG-C anode (Fig. 6a, b, and Supplementary Fig. 14b). The VC electrolyte induced the build-up of a thick SEI on the outermost anode surface (Fig. 6f), and the anode particles lost their electronic connection. This finding suggests that VC does not preserve the SiG-C anode structure properly in the full cell, and the lithium-storage ability of the anode is greatly diminished. The beneficial effects of the VC + APFS electrolyte on the interfacial stabilization of the SiG-C anode and the suppression of dissolved Ni from the cathode and Ni plating on the anode are illustrated in Fig. 6c. Uncontrolled CEI on the cathode with VC induces micro-cracking of NCM secondary particles, resulting in impregnation of the electrolyte inside the cathode particle. In

contrast, the VC + APFS electrolyte constructed a stable CEI on NCM811 cathode and robust SEI on SiG-C anode and thereby Ni deposition-induced SEI damage was mitigated.

Improved CEI stability by VC + APFS electrolyte. In addition to the beneficial effect of VC + APFS on the SEI quality of SiG-C anodes in full cells, a significant role of VC + APFS in modifying the CEI of NCM811 cathodes was observed by XPS (Fig. 7). The significant difference between the XPS studies of NCM811 cathodes with VC and VC + APFS is based on S 2p spectra. Residual APFS predominately contributed to the CEI formation through the oxidative decomposition at a charge voltage of 4.2 V after contributing to the sulfur-rich SEI formation below 4.0 V, and the relative fraction of sulfur-containing species increased in the CEI (Fig. 7b). A possible CEI structure is shown in Fig. 1. The prominently increased fraction of metal (M)–O species on the cathode with VC electrolyte at a charge voltage of 3 V may be attributed to the loss of cathode surface coverage by the CEI instability. In contrast to the cathode with VC electrolyte, discernible change in the M–O peak of the cathode with VC + APFS electrolyte did not appear. This finding suggests that APFS promotes the CEI, which is sufficiently electrochemically strong to protect the NCM811 cathode. A computational study suggests that APFS additive deactivates PF_5 producing corrosive HF by undesirable reaction with a trace of moisture in the electrolyte (Fig. 8a). The heat of reaction was increased, and the energy barrier was raised in the presence of APFS. The mitigation of HF generation in the electrolyte may help maintain the interfacial layers on the SiG-C anode and NCM811 cathode stably during cycling.

The role of APFS in deactivating PF_5 molecules was also evidenced by the ^{19}F NMR results (Fig. 8b and c). The relative intensity of the HF peak at − 191 ppm was reduced from 24.9–13.1% by introducing APFS into the electrolyte. Additionally, the relative intensity of the corresponding peaks of $PO_2F_2^-$ at − 80.8 ppm and − 83.4 ppm was decreased. This is because of the deactivation ability of APFS, which forms the complex with PF_5. The undesirable formation of acid compounds (HF and HPO_2F_2) aggravates the leaching of transition metal (TM) ions from the NCM811 cathode at elevated temperatures. The dissolved TM ions migrate toward the lithiated anode when a fully charged full cell is stored at 60 °C. The VC + APFS-containing cell exhibited a discharge capacity retention of 86.7% (171.8 mAh g^{-1}), which was comparable to that of the VC + FEC-containing cell (171.7 mAh g^{-1} (86.1%)) (Supplementary Fig. 15a and b). In contrast, the VC + APFS electrolyte showed improved capacity retention and recovery with reduced cell resistance after storage at 60 °C for 20 days compared with other electrolytes (Supplementary Fig. 15c and d). Because the capacity loss after high-temperature storage is associated with Li-ion extraction from the lithiated SiG-C anode, it is logical that the VC + APFS-promoted SEI is robust enough to maintain the charged state of the SiG-C anode without severe thickening of the SEI, which causes cell resistance. The quantity of dissolved TM from the delithiated NCM811 cathode with VC- and VC + APFS-induced CEI in contact with 1 M $LiPF_6$ EC/EMC/DEC (25/45/30 vol%) for 3 days at 60°C was examined through the inductively coupled plasma optical emission spectrometry (ICP-OES) analysis. Ni ions dissolved from the delithiated NCM811 was significantly reduced in the APFS electrolyte (Supplementary Fig. 16). The onset temperature of the exothermic peak of APFS-applied delithiated cathodes was considerably delayed compared with that of the VC and VC + FEC electrolytes, and the total heat released

was also reduced to 0.88 kJ g^{-1}, confirming that the CEI formed by APFS effectively mitigated the exothermic surface reaction of the NCM particles (Supplementary Fig. 17a). In addition, the combination of APFS with VC improved the thermal stability of the SEI and lithiated SiG-C anodes (Supplementary Fig. 17b). The structural stability of NCM811 cathodes by VC, VC + FEC, and VC + APFS was examined (Fig. 9a–d and Supplementary Fig. 18c and d). Notably, the intergranular cracking of the NCM811 cathode particles was effectively suppressed in the VC + APFS electrolyte compared with VC and VC + FEC electrolytes. This finding reveals that the CEI formed by VC + APFS helps enable the homogeneous delithiation and lithiation of NCM811 primary particles without severe intergranular cracking. Conversely, the CEI formed on the cathode with VC electrolyte did not lead to uniform delithiation and lithiation of NCM811 primary particles and hence, severe morphological degradation of NCM particles occurred (Fig. 9a and b). Although the VC + FEC electrolyte shows a better cycle life at 25°C and 45°C than VC, the thickening of the cathode by accumulating decomposed electrolyte byproducts still occurs.

The beneficial effect of APFS mitigating the irreversible phase transformation of NCM811 cathodes at the atomic level was confirmed through scanning transmission electron microscopy (STEM) with fast Fourier transform (FFT) and electron energy loss spectroscopy (EELS) analysis (Fig. 9e–h). The thickening of the phase transformation layer to the rock-salt phase in the R_3*m* space group impedes the Li-ion transport into the layered structure of the cathode and decreases the Li-storage capability of the cathode. APFS drastically reduced the phase transformation thickness to 3.1 nm while maintaining the layered structure at site E (Fig. 9f). Notably, FEC, which showed similar discharge capacity retention with APFS after 100 cycles (Supplementary Fig. 19a), did not mitigate the severe phase transformation of the cathode. The interfacial stabilization effect of APFS was also evidenced by EELS studies on the distinguishing oxidation state of TM of the NCM811 cathode (Fig. 9g and h). The variation in the oxidation state of TM ions was characterized by two indices, the energy loss difference (ΔE) of the O K-edge, and the intensity ratio (L_3/L_2) of TM ions[37]. The ΔE of the O K-edge is defined as the energy loss change from the main-edge peak (~ 540 eV) to pre-edge peaks (~ 530 eV). Because the O K-edge peaks demonstrate the local vacant 3d state of TMs, their movement to lower energy loss represents the oxidation of the TM ion. The VC + APFS electrolyte led to a high ΔE value, indicating the mitigation of the reduction of Ni^{4+} ions to lower valance states (Ni^{2+} and Ni^{3+}) on the surface[38–40] (Supplementary Fig. 19d). In addition, a distinct O K-edge peak appeared at a relatively low depth for the NCM811 cathode cycled with VC + APFS electrolyte, indicating a low level of oxygen loss (Fig. 9g, h, and Supplementary Fig. 19c). Notably, the Ni^{2+} ions formed in delithiated states are prone to migration into the vacant Li slabs, causing undesired Li/Ni cation mixing at the NCM811 cathode during cycling. The Ni L_3/L_2 ratio decreased more rapidly from the surface to bulk in the re-lithiated state of the NCM811 cathode with VC + APFS electrolyte after 100 cycles (Supplementary Fig. 19e). This result reveals that the thickening of inactive rock-salt structure induced by the migration of Ni^{2+} ions into the Li slabs at the surface region was effectively mitigated by the electrochemically robust APFS-derived CEI on the NCM811 cathode. The X-ray diffraction patterns implied that the inhomogeneous VC-derived CEI induced unwanted Li consumption at the cathode and caused irreversible structural changes in the cathode lattice

(Supplementary Fig. 20a–c). Conversely, the APFS-modified CEI effectively suppressed the undesired electrolyte oxidation at the NCM811 cathode and improved the mechanical integrity of the cathode.

Discussion

In this study, we demonstrated the action mechanism of the APFS to achieve remarkable characteristics of SEI and CEI in SiG-C/NCM811 full cells with practical mass loading. The introduction of APFS in VC electrolyte led to the creation of SEI with LiF-rich and polymeric species accommodating severe volume changes of the SiG-C anode during electrochemical cycles. The synthetic fluorosulfate additive also contributed to the creation of thermally robust sulfur-containing SEI and CEI. The sulfur-containing CEI restrained further electrolyte oxidation at the cathode, effectively reduced the generation of exothermic heat from the delithiated cathode at high temperatures, and suppressed TM dissolution from the NCM811 cathode. Moreover, the PF_5 deactivation ability of the APFS contributed to mitigating interfacially induced instability of the NCM811 cathode and SiG-C anode. This study may lead to new design guidance for electrolyte additives and can provide opportunities to replace conventional electrolyte additives, including FEC with thermal and chemical instability in $LiPF_6$-based electrolytes.

Methods

General information for synthesis. All chemicals were purchased from standard suppliers and used without further purification. Merck silica gel 90 (size range = 0.040–0.063 mm) was utilized for flash column chromatography. ^1H, ^{13}C, and ^{19}F NMR spectra were acquired on a Bruker Avance III HD 400 (400 MHz for ^1H; 101 MHz for $^{13}C\{^1H\}$, 376 MHz for $^{19}F\{^1H\}$). α,α,α-Trifluorotoluene (δ = -63.72, dimethyl sulfoxide (DMSO)-d_6) was employed as an internal standard for $^{19}F\{^1H\}$ NMR spectra.

Synthesis of 4-(allyloxy)phenol [41] . Allyl bromide (4.50 mL, 52.1 mmol) was introduced into a suspension of hydroquinone (10.0 g, 90.8 mmol) and potassium carbonate (2.10 g, 15.2 mmol) in acetonitrile (20 mL) at room temperature (RT, 25°C), and the reactor was heated for 12 hrs to reflux. The blends were then chilled down to RT and purified by flash column chromatography (dichloromethane : ethyl acetate = 50 : 1) to afford a grayish solid (2.48 g, 32%). ^1H NMR (400 MHz, $CDCl_3$) δ 6.94–6.71 (m, 4H), 6.14–5.97 (m, 1H), 5.47–5.34 (m, 1H), 5.34–5.21 (m, 1H), and 5.00 (s, 1H), 4.57–4.41 (m, 2H). ^{13}C NMR (101 MHz, $CDCl_3$) δ 152.8, 149.7, 133.6, 117.8, 116.2, 116.1, and 69.8.

Synthesis of 4-(allyloxy)phenyl 1 H **-imidazole-1-sulfonate [29]** . 4-(Allyloxy)phenol (4.50 g, 30.0 mmol) was introduced into a suspension of cesium carbonate (4.88 g, 15.0 mmol) and 1,1'-sulfonyldiimidazole (8.91 g, 45.0 mmol) in THF (45 mL). After stirring at RT for 12 h, the mixture was purified by flash column chromatography (n-hexane:ethyl acetate = 2:1) to afford a colorless oil (7.78 g, 93%). ^1H NMR (400 MHz, $CDCl_3$) δ 7.79–7.65 (m, 1H), 7.28 (t, J = 1.4 Hz, 1H), 7.15 (dd, J = 1.6, 0.8 Hz, 1H), 6.86–6.78 (m, 4H), 6.00 (ddt, J = 17.2, 10.6, 5.3 Hz, 1H), 5.44–5.26 (m, 2H), and 4.49 (dt, J = 5.3, 1.5 Hz, 2H). ^{13}C NMR (101 MHz, $CDCl_3$) δ 158.4, 142.5, 137.7, 132.6, 131.4, 122.4, 118.4, 118.3, 115.6, and 69.3.

Synthesis of 4-(allyloxy)phenyl fluorosulfate [29] . Silver (I) fluoride (6.34 g, 50.0 mmol) was introduced into a suspension of 4-(allyloxy)phenyl 1*H*-imidazole-1-sulfonate (7.78 g, 27.8 mmol) in acetonitrile (100 mL). After stirring for 12 hrs at 80°C, the mixed solutions were purified to afford a colorless oil (5.80 g, 90%) by flash column chromatography (n-hexane:ethyl acetate = 4:1). ^{1}H NMR (400 MHz, DMSO-d_6) δ 7.51 (d, J = 9.2 Hz, 2H), 7.22–7.04 (m, 2H), 6.03 (ddt, J = 17.2, 10.5, 5.2 Hz, 1H), 5.40 (dd, J = 17.3, 1.6 Hz, 1H), 5.28 (dd, J = 10.5, 1.4 Hz, 1H), and 4.62 (d, J = 5.2 Hz, 2H). ^{19}F NMR (377 MHz, DMSO-d_6) δ 34.8.

Preparation of electrodes and electrolytes. The SiG-C anode was fabricated with 96 wt% active material comprising 30 wt% graphite and 70 wt% Si/C, 1 wt% carbon black, and a binder with 2 wt% styrene-butadiene rubber and 1 wt% carboxymethyl cellulose. The mass loading and thickness of the SiG-C anode were 10.90 mg cm^{-2} and 78 μm, respectively. The cathode was fabricated by mixing 95.8 wt% $LiNi_{0.8}Co_{0.1}Mn_{0.1}O_2$ (NCM811), 2 wt% carbon black, and 2.2 wt% poly(vinylidene fluoride) binder. The mass loading and thickness of NCM811 cathode were 20.5 mg cm^{-2} and 72 μm, respectively. Before utilization, all the electrodes were vacuum-dried for 10 h at 110°C. Hyundai Motor Co., Ltd supplied all the electrodes.

The VC (Enchem) electrolyte was prepared by incorporating 1 wt% VC with 1 M lithium hexafluoro phosphate ($LiPF_6$, > 99.9% Soulbrain Co., Ltd.) in EC/EMC/DEC (25:45:30 vol%) (> 99.9%, Sigma Aldrich). For comparison, 2 wt% FEC (Enchem) or 0.5 wt% APFS was added to the VC-containing electrolyte. The electrolytes were handled with calcium hydride (CaH_2) to reduce the moisture. The Karl Fischer titration (C30, Mettler Toledo) was conducted for titration of all electrolytes to ensure that the trace moisture was less than 10 ppm.

Electrochemical measurements. 2032 coin-type full cells, which were manufactured in a glove box filled with Ar-gas (O_2 and H_2O < 1.0 ppm), were cycled at 45°C and 1 C after precycling from 2.5 V to 4.2 V at 0.1 C and 25 ℃ using a battery performance evaluation device (TOSCAT-3100, TOYO System Co., LTD.). For comparison of electrochemical reduction behaviors of electrolyte additives, Si/C-graphite (SiG-C)/Li half-cells were precycled from 1.5 V to 0.05 V vs. Li/Li$^+$ at C/20. An Al_2O_3-coated polyethylene membrane with 49.2% porosity and 15.1 μm thickness was employed as a separator. The cells were stored at 60°C for 20 days to explore their self-discharge properties, and the cell impedance was measured by the direct current internal resistance method at the state of charge 50.

Characterization. For analysis, all procedures were conducted in a glove box with full of inert argon gas. The cells were disassembled, and dimethyl carbonate was used for elimination of the remaining electrolyte from the electrodes. The elemental composition of the SEI and CEI layers was identified by XPS (ESCALAB 250Xi System, Thermo Fisher Scientific) analysis, which was conducted using Al-ka (hv = 1486 eV) X-ray under ultrahigh vacuum conditions. The samples of the cycled electrodes for XPS measurements were packed in a tight aluminum pouch in a glovebox and transferred to the XPS chamber before measurement to minimize contamination by air and moisture. The decomposition of electrolyte additives at different charged states during precycling and the amount of $PO_2F_2^-$ with HF generation

after storing the electrolyte were examined by 400 MHz ^{1}H NMR spectroscopy (AVANCE III HD, Bruker) using THF-d_8 (99.5%, NMR grade, BK Instruments Inc.). The relative amounts of $PO_2F_2^-$ and HF generated during the storage of the electrolyte solutions (at 25°C for 10 days) were calculated based on the exact amount of 1 wt% hexafluorobenzene (internal standard) for ^{19}F-NMR analysis.

The mechanical property of the VC- and VC + APFS-promoted SEI on the SiG-C anode was examined by comparing their Young's modulus through the contact mode of AFM (MultiMode V, Veeco). FT-IR spectroscopy (670/620-IR Series, Varian Inc.) was performed to analyze the polymeric species formed by the co-decomposition of VC + APFS. Morphological changes of the SiG-C anodes and NCM811 cathodes with VC, VC + FEC, and VC + APFS were explored using SEM (SU8230, Hitachi). The high-angle annular dark-field STEM (HAADF-STEM, Titan G2 60–300, FEI) analysis were conducted using focused ion beam (FIB, Helios Nanolab 450, FEI) to determine the phase transition behavior of NCM811 cathode with different electrolyte and subsequent EELS was analyzed for evaluating the oxidation state of TM ions. The EELS profiles were collected from the surface to bulk electrode at a 1-nm interval.

Computational details. In order to investigate the orbital energy levels, deformation energies, F dissociation energies, and reaction mechanisms, DFT calculations were performed with the DMol^3 program[42,43]. All calculations were performed in an implicit environment using the conductor-like screening model (COSMO) while using an estimated dielectric constant (= 10.757) of the solvent mixture (EC/DEC/EMC (25/30/45 vol%))[44]. A detailed description of DFT calculations is provided in the Supplementary Information.

Data availability

The authors declare that the main data supporting the findings of this study are available within the article and its Supplementary Information. All other additional information is available from the corresponding authors upon reasonable request.

Declarations

Acknowledgements

This work was supported by settlement research funds for newly hired faculty of Korea Advanced Institute of Science and Technology (KAIST; project number G04210040) and by the Hyundai Motor Company. This research was partly supported by the Technology Development Program to Solve Climate Change of the National Research Foundation (NRF) funded by the Ministry of Science, ICT & Future Planning (2021M1A2A2038148). The computational resources were provided by UNIST-HPC and KISTI (KSC-2020-INO-0030).

Author contributions

K.K., Y.-S.L, S.Y.H., S.K.K., and N.-S.C. conceived and designed the projects. H.N. and H.M. conducted characterizations and electrochemical measurements. M.P.K., M.H.J., J.-H.C., and S.Y.H. synthesized the electrolyte additives. S.M.L. and H.K. executed the density functional theory calculations. H.M., H.N., M.P.K., S.M.L., S.Y.H., S.K.K., and N.-S.C. wrote the manuscript. H.M., H.N., M.P.K., and S.M.L. contributed equally to this work. All authors analyzed the data and contributed to the discussion.

Competing interests

The authors declare no competing interests.

References

1. Goodenough, J. B. & Kim, Y. Challenges for rechargeable Li batteries. Chem. Mater. **22**, 587–603 (2010).
2. Xu, K. Electrolytes and interphases in Li-ion batteries and beyond. Chem. Rev. **114**, 11503–11618 (2014).
3. Li, M., Lu, J., Chen, Z. & Amine, K. 30 Years of lithium-ion batteries. Adv. Mater. **30**, 1800561 (2018).
4. Tarascon, J. M. & Armand, M. Issues and challenges facing rechargeable lithium batteries. Nature **414**, 359–367 (2001).
5. Choi, N.-S. *et al.* Challenges facing lithium batteries and electrical double-layer capacitors. Angew. Chem. Int. Ed. **51**, 9994–10024 (2012).
6. Bak, S. M. *et al.* Structural changes and thermal stability of charged $LiNi_xMn_yCo_zO_2$ cathode materials studied by combined in situ time-resolved XRD and mass spectroscopy. ACS Appl. Mater. Interfaces **6**, 22594–22601 (2014).
7. Bak, S. M. *et al.* Correlating structural changes and gas evolution during the thermal decomposition of charged $Li_xNi_{0.8}Co_{0.15}Al_{0.05}O_2$ cathode materials. Chem. Mater. **25**, 337–351 (2013).
8. Ryu, J., Hong, D., Lee, H. W. & Park, S. Practical considerations of Si-based anodes for lithium-ion battery applications. Nano Res. **10**, 3970–4002 (2017).
9. Chae, S., Choi, S.-H., Kim, N., Sung, J. & Cho, J. Integration of graphite and silicon anodes for the commercialization of high-energy lithium-ion batteries. Angew. Chem. Int. Ed. **59**, 110–135 (2020).
10. Obrovac, M. N. & Christensen, L. Structural changes in silicon anodes during lithium insertion/extraction. Electrochem. Solid-State Lett. **7**, A93 (2004).
11. Soto, F. A., Martinez de la Hoz, J. M., Seminario, J. M. & Balbuena, P. B. Modeling solid-electrolyte interfacial phenomena in silicon anodes. Curr. Opin. Chem. Eng. **13**, 179–185 (2016).
12. Kim, K. *et al.* Understanding the thermal instability of fluoroethylene carbonate in $LiPF_6$-based electrolytes for lithium ion batteries. Electrochim. Acta **225**, 358–368 (2017).
13. Aurbach, D. *et al.* On the use of vinylene carbonate (VC) as an additive to electrolyte solutions for Li-ion batteries. Electrochim. Acta **47**, 1423–1439 (2002).

14. Ota, H., Sakata, Y., Inoue, A. & Yamaguchi, S. Analysis of vinylene carbonate derived SEI layers on graphite anode. J. Electrochem. Soc. **151**, A1659 (2004).
15. Song, H. S. *et al.* Effect of vinylene carbonate as electrolyte additive on cycling performance of $LiFePO_4$/graphite cell at elevated temperature. Trans. Nonferrous Met. Soc. China English Ed. **24**, 723–728 (2014).
16. Rezqita, A., Sauer, M., Foelske, A., Kronberger, H. & Trifonova, A. The effect of electrolyte additives on electrochemical performance of silicon/mesoporous carbon (Si/MC) for anode materials for lithium-ion batteries. Electrochim. Acta **247**, 600–609 (2017).
17. Wang, J. P., Wang, C. Y., Yang, D. J., Wu, N. N. & Tian, W. H. Effects of electrolytes additive on the electrochemical performance of Si/disordered carbon composite anode for lithium-ion batteries. *IEEE Transportation Electrification Conference and Expo, ITEC Asia-Pacific 2014 - Conference Proceedings* **54**, (2014).
18. Wu, S. & Huang, A. Effects of Tris(Pentafluorophenyl) Borane (TPFPB) as an Electrolyte Additive on the Cycling Performance of $LiFePO_4$ Batteries. J. Electrochem. Soc. **160**, A684–A689 (2013).
19. Han, J.-G. *et al.* Unsymmetrical fluorinated malonatoborate as an amphoteric additive for high-energy-density lithium-ion batteries. Energy Environ. Sci. **11**, 1552–1562 (2018).
20. Nölle, R., Achazi, A. J., Kaghazchi, P., Winter, M. & Placke, T. Pentafluorophenyl isocyanate as an effective electrolyte additive for improved performance of silicon-based lithium-ion full cells. ACS Appl. Mater. Interfaces **10**, 28187–28198 (2018).
21. Lee, S. J. *et al.* A bi-functional lithium difluoro(oxalato)borate additive for lithium cobalt oxide/lithium nickel manganese cobalt oxide cathodes and silicon/graphite anodes in lithium-ion batteries at elevated temperatures. Electrochim. Acta **137**, 1–8 (2014).
22. Park, S. *et al.* Replacing conventional battery electrolyte additives with dioxolone derivatives for high-energy-density lithium-ion batteries. Nat. Commun. **12**, 1–12 (2021).
23. Pires, J. *et al.* Role of propane sultone as an additive to improve the performance of a lithium-rich cathode material at a high potential. RSC Adv. **5**, 42088–42094 (2015).
24. Zhang, B. *et al.* Role of 1,3-propane sultone and vinylene carbonate in solid electrolyte interface formation and gas generation. J. Phys. Chem. C **119**, 11337–11348 (2015).
25. Xia, J. *et al.* Combinations of ethylene sulfite (ES) and vinylene carbonate (VC) as electrolyte additives in $Li(Ni_{1/3}Mn_{1/3}Co_{1/3})O_2$/Graphite Pouch Cells. ECS Meet. Abstr. **MA2014-02**, 296–296 (2014).
26. Janssen, P. *et al.* 1,3,2-Dioxathiolane-2,2-dioxide as film-forming agent for propylene carbonate based electrolytes for lithium-ion batteries. Electrochim. Acta **125**, 101–106 (2014).
27. Liao, Y. *et al.* Synergistic effect of electrolyte additives on the improvement in interfacial stability between ionic liquid based gel electrolyte and $LiFePO_4$ cathode. Solid State Ionics **329**, 31–39 (2019).

28. Lee, S. J. *et al.* Effect of lithium bis(oxalato)borate additive on electrochemical performance of $Li_{1.17}Ni_{0.17}Mn_{0.5}Co_{0.17}O_2$ cathodes for lithium-ion batteries. J. Electrochem. Soc. **161**, A2012–A2019 (2014).
29. Kwon, Y. Do *et al.* Synthesis of ^{18}F-labeled aryl fluorosulfates via nucleophilic radiofluorination. Org. Lett. **22**, 5511–5516 (2020).
30. Xue, W. *et al.* FSI-inspired solvent and “full fluorosulfonyl” electrolyte for 4 V class lithium-metal batteries. Energy Environ. Sci. **13**, 212–220 (2020).
31. Okuno, Y., Ushirogata, K., Sodeyama, K. & Tateyama, Y. Decomposition of the fluoroethylene carbonate additive and the glue effect of lithium fluoride products for the solid electrolyte interphase: An ab initio study. Phys. Chem. Chem. Phys. **18**, 8643–8653 (2016).
32. Zhang, X. *et al.* Self-Suppression of lithium dendrite in all-solid-state lithium metal batteries with poly(vinylidene difluoride)-based solid electrolytes. Adv. Mater. **31**, 1–9 (2019).
33. Parsaee, F. *et al.* Radical philicity and its role in selective organic transformations. Nat. Rev. Chem. **5**, 486–499 (2021).
34. Zhang, H. *et al.* Room temperature formation of organic-inorganic lead halide perovskites: design of nanostructured and highly reactive intermediates. J. Mater. Chem. A **5**, 3599–3608 (2017).
35. Yamaguchi, T., Asada, T., Hayashi, H. & Nakamura, N. Dependence of the packing structure of mesogenic groups on the flexible spacer length of liquid crystalline side-chain polymers. Macromolecules **22**, 1141–1144 (1989).
36. Collet, J. P., Shuman, H., Ledger, R. E., Lee, S. & Weisel, J. W. The elasticity of an individual fibrin fiber in a clot. *Proc. Natl. Acad. Sci. U. S. A.* **102**, 9133–9137 (2005).
37. Hwang, S. *et al.* Determination of the mechanism and extent of surface degradation in Ni-based cathode materials after repeated electrochemical cycling. APL Mater. **4**, 0–7 (2016).
38. Graetz, J., Ahn, C. C., Yazami, R. & Fultz, B. An electron energy-loss spectrometry study of charge compensation in $LiNi_{0.8}Co_{0.2}O_2$. J. Phys. Chem. B **107**, (2003).
39. Xu, B., Fell, C. R., Chi, M. & Meng, Y. S. Identifying surface structural changes in layered Li-excess nickel manganese oxides in high voltage lithium ion batteries: A joint experimental and theoretical study. Energy Environ. Sci. **4**, (2011).
40. Gu, M. *et al.* Nanoscale phase separation, cation ordering, and surface chemistry in pristine $Li_{1.2}Ni_{0.2}Mn_{0.6}O_2$ for Li-ion batteries. Chem. Mater. **25**, 2319–2326 (2013).
41. Guo, J., Mayers, P. C., Breault, G. A. & Hunter, C. A. Synthesis of a molecular trefoil knot by folding and closing on an octahedral coordination template. Nat. Chem. **2**, 218–222 (2010).
42. Delley, B. An all-electron numerical method for solving the local density functional for polyatomic molecules. J. Chem. Phys. **92**, 508–517 (1990).
43. Delley, B. From molecules to solids with the $DMol^3$ approach. J. Chem. Phys. **113**, 7756–7764 (2000).

44. Klamt, A. & Schüürmann, G. COSMO: A new approach to dielectric screening in solvents with explicit expressions for the screening energy and its gradient. J. Chem. Soc. Perkin Trans. **2** 799–805 (1993).

Figures

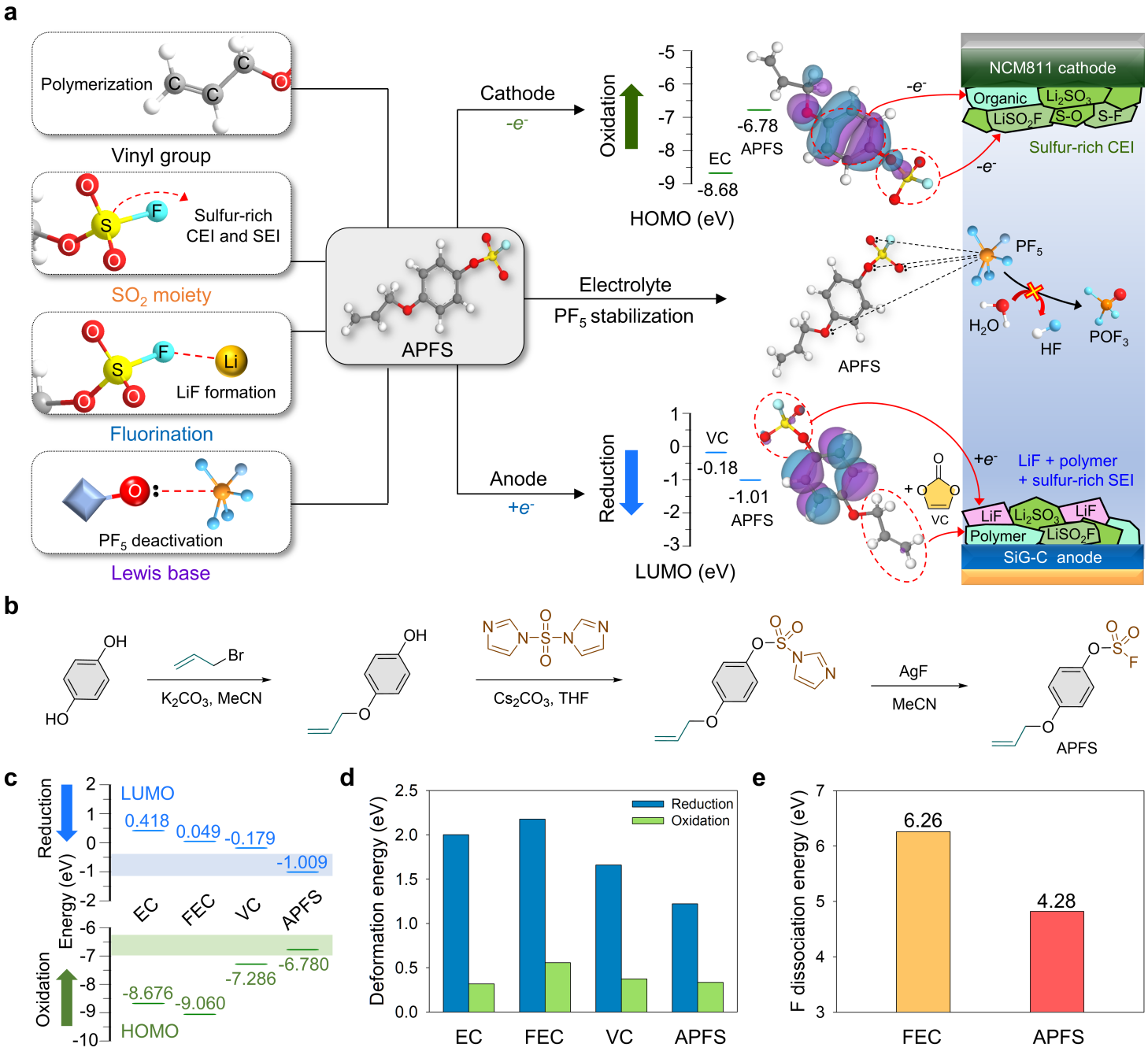

Figure 1

APFS additive for the construction of interfacial layers on the NCM811 cathode and SiG-C anode. a, Schematic diagram of the construction of SEI on the SiG-C anode and CEI on the NCM811 cathode. The APFS radical is formed through hydrogen atom reaction (HAT) upon electrochemical reduction at the

anode. **b,** Synthesis of APFS additive. **c,** HOMO and LUMO energy levels, **d,** deformation energy, and **e,** F dissociation energy of EC, FEC, VC, and APFS.

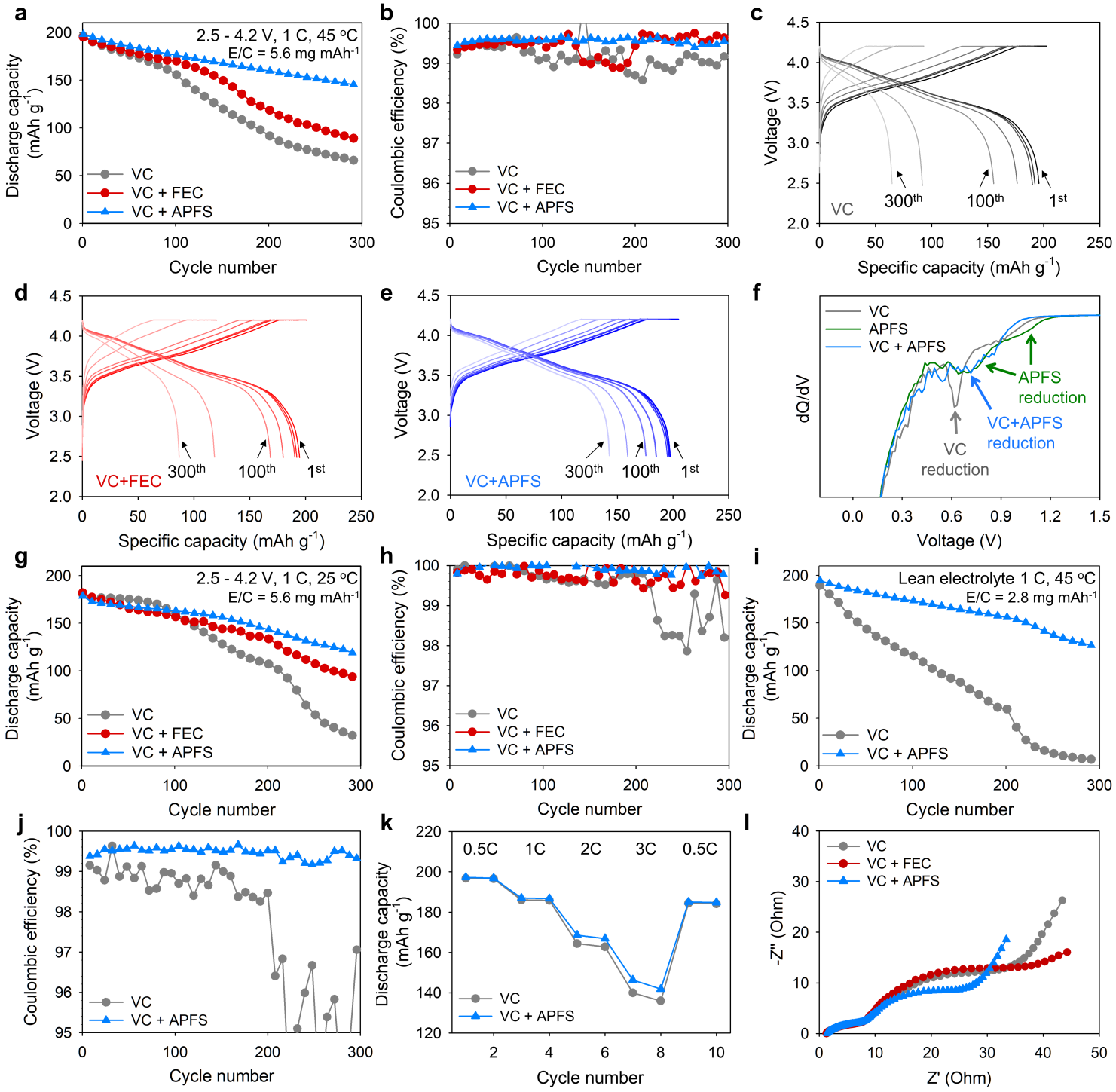

Figure 2

Electrochemical performance of APFS additive. a, The cycle behavior and **b,** Coulombic efficiency of SiG-C/NCM811 full cells at 45 °C. Selected voltage profile curves of SiG-C/NCM811 full cells with **c,** VC, **d,**

VC+FEC, or **e,** VC+APFS electrolyte. **f,** The dQ/dV plot of the SiG-C/Li half-cell with VC, VC+APFS, and APFS electrolytes. **g,** The cycle behavior and **h,** Coulombic efficiency of SiG-C/NCM811 full cells at 25 °C. **i,** The cycle behavior and **j,** Coulombic efficiency of SiG-C/NCM811 full cells at 45 °C under lean electrolyte conditions. **k,** Rate capability of SiG-C/NCM811 full cells at different charging rates with a fixed discharginig rate of C/10. **l,** Electrochemical impedance spectroscopy results of SiG-C/NCM811 full cells after precycling.

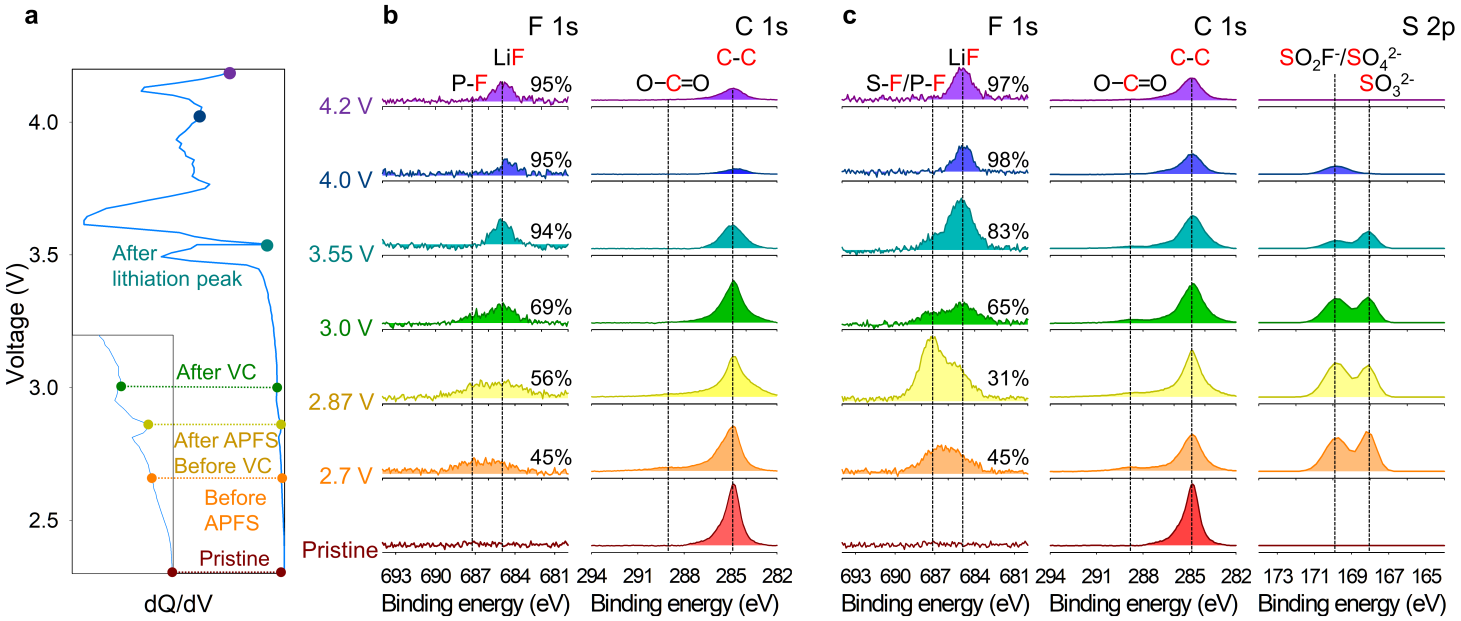

Figure 3

XPS analysis to confirm the fluorosulfate-containing SEI formation on the anode. a, The dQ/dV plot of the SiG-C/NCM811 full cell with the VC+APFS electrolyte during the charge process of precycling at C/10. The inset represents the enlarged region of voltages linked to the SEI creation during the charge process of precycling. **b,** F 1s and C 1s XPS results of SiG-C anodes with VC. **c,** F 1s, C 1s, and S 2p XPS results of the SiG-C anodes with the VC+APFS electrolyte.

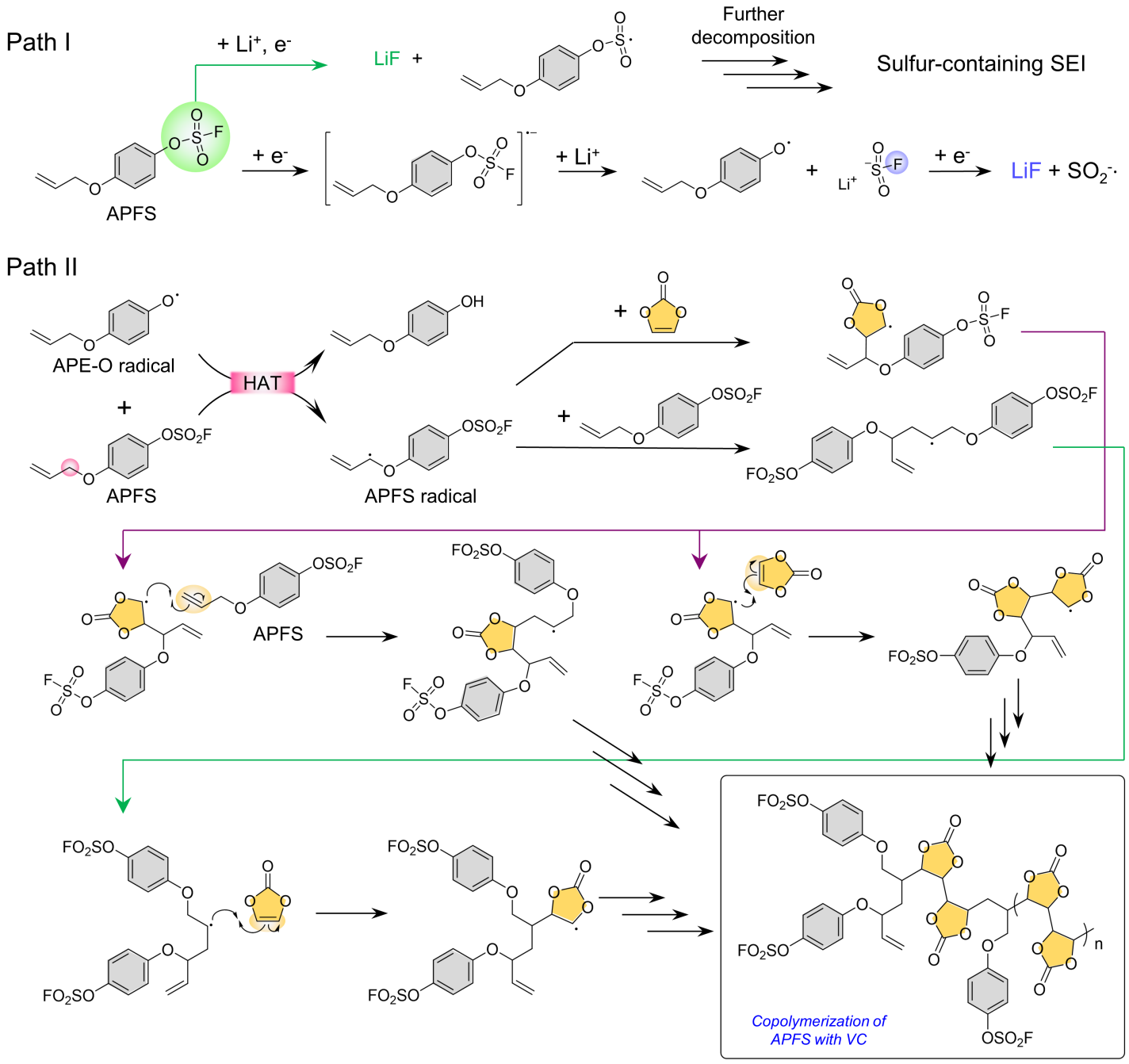

Figure 4

The proposed reductive, radical pathways of APFS with VC on the surface of the anode.

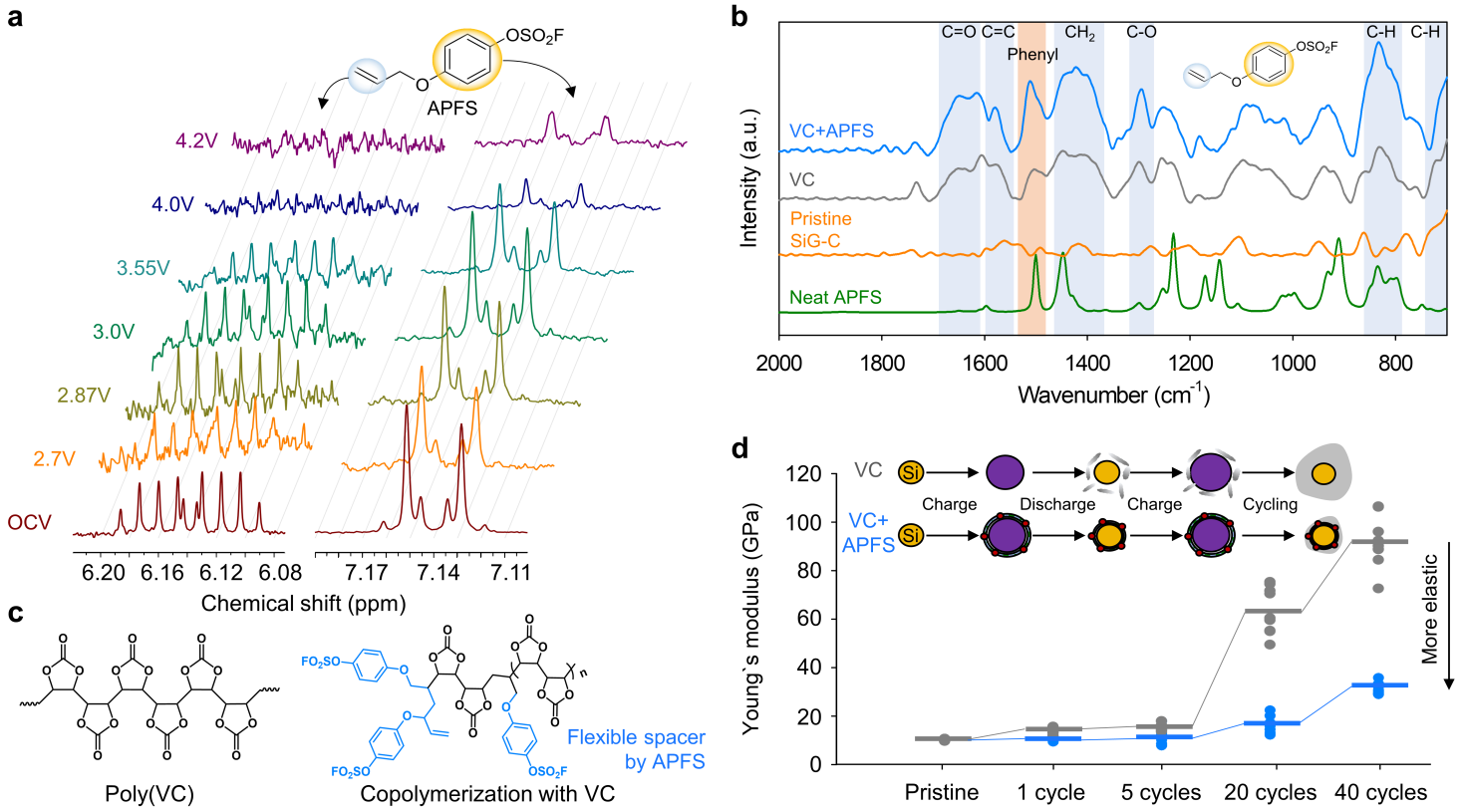

Figure 5

Elucidation of APFS decomposition to build-up of flexible SEI on the SiG-C anode. a, ^{1}H NMR (400 MHz, THF-d_8) spectra of the APFS additive upon the first charge at selected voltages—open circuit voltage (OCV): pristine state, 2.7 V: before the reduction of the APFS additive, 2.87 V: after the APFS reduction and before the VC reduction, 3.0 V: after the VC reduction, 3.55 V: after lithiation of the SiG-C anode, 4.0 V: after phase transition of the NCM811 cathode both from H1 to M and from M to H2, and 4.2 V: after phase transition of NCM811 from H2 to H3. **b,** FT-IR of APFS, the pristine SiG-C anode, and the anode precycled with VC and VC+APFS. **c,** Polymer SEI formed by APFS. **d,** Young's modulus changes of the SiG-C anode during the repeated cycles of SiG-C/NCM811 full cells (gray: VC electrolyte, blue: VC+APFS electrolyte).

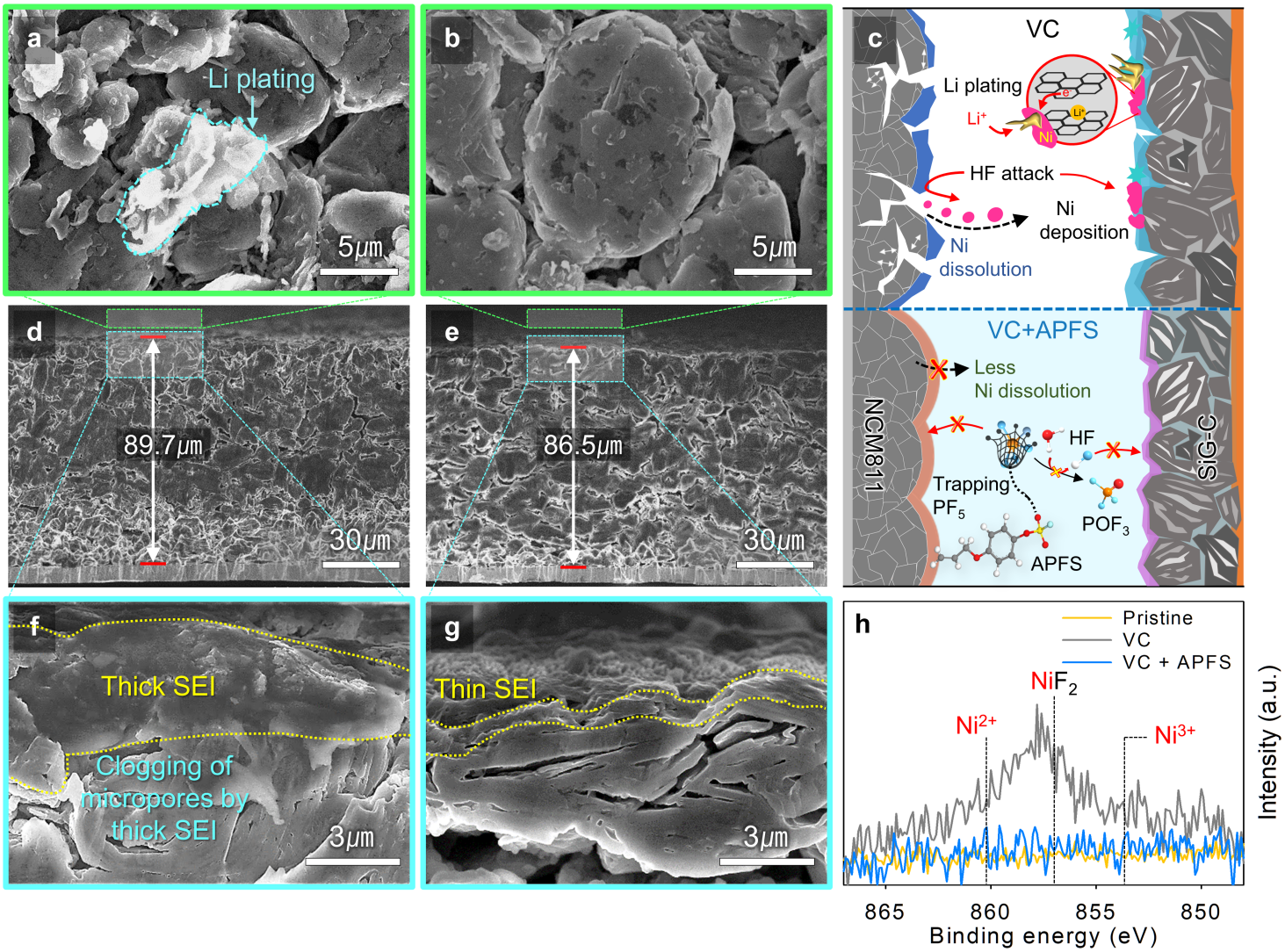

Figure 6

Characterization of SiG-C anodes with and without the VC+APFS electrolyte. Cross-sectional and surface morphologies of SiG-C anodes obtained from SiG-C/NCM811 full cells after 100 cycles at 45 °C with **a, d, f,** VC or **b, e, g,** VC+APFS electrolyte. **c,** Schematic representation for Ni dissolution behavior from NCM811 cathode and Ni plating on SiG-C anode with the VC or VC+APFS electrolyte. **h,** XPS Ni 2p spectra of SiG-C anodes after 100 cycles at 1 C and 45 °C.

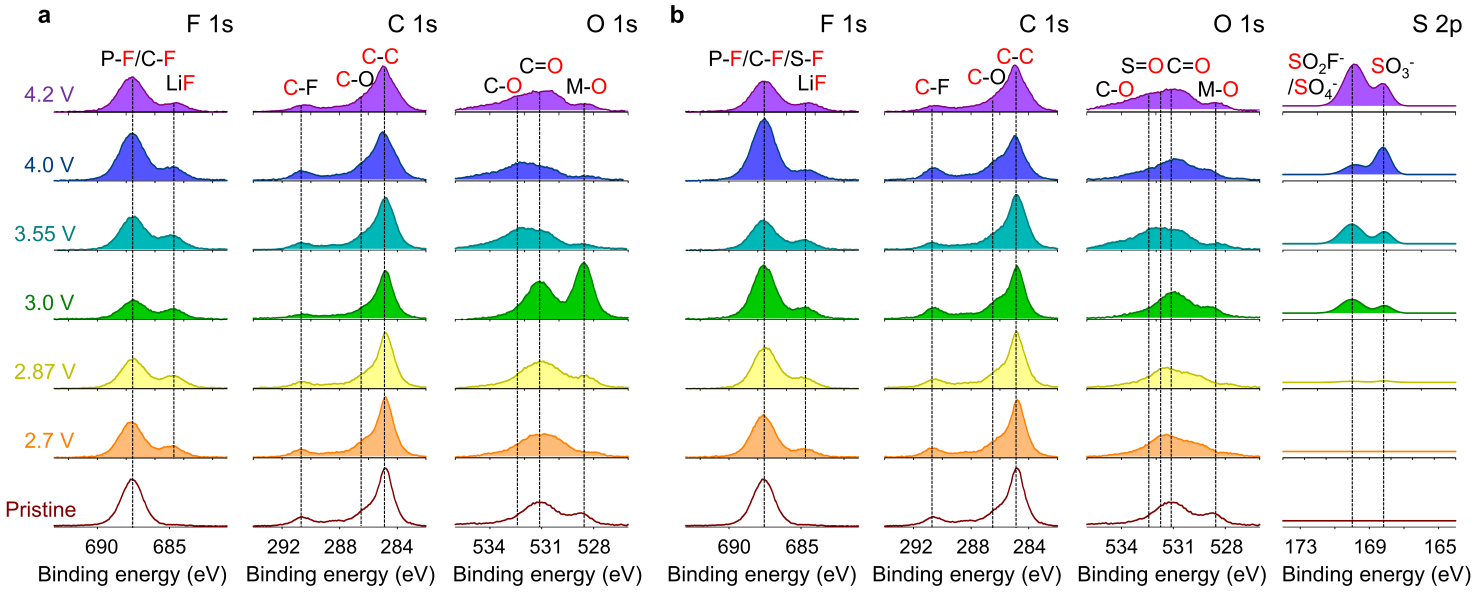

Figure 7

Surface chemistry of NCM811 cathodes during the first charging process. XPS analysis results of NCM811 cathodes containing **a,** VC or **b,** VC+APFS electrolyte at different charged states.

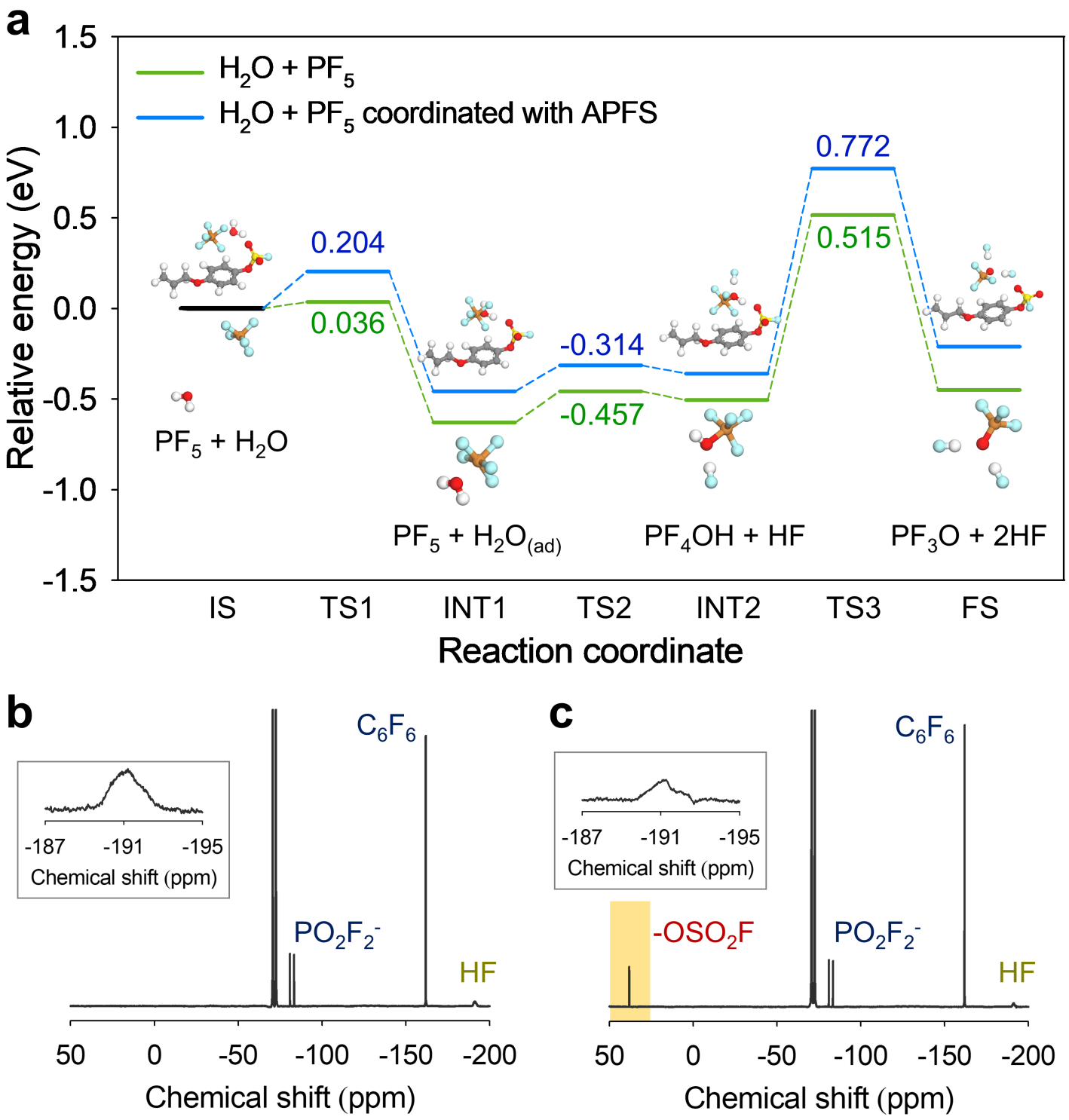

Figure 8

APFS for deactivating PF_5. a, Relative energies of PF_5 hydrolysis with and without the APFS additive in the electrolyte at the initial state (IS), transition states (TS1, 2, and 3), intermediate states (INT1 and 2), and final state (FS). ^{19}F NMR spectra of the electrolytes **b,** with VC or **c,** APFS.

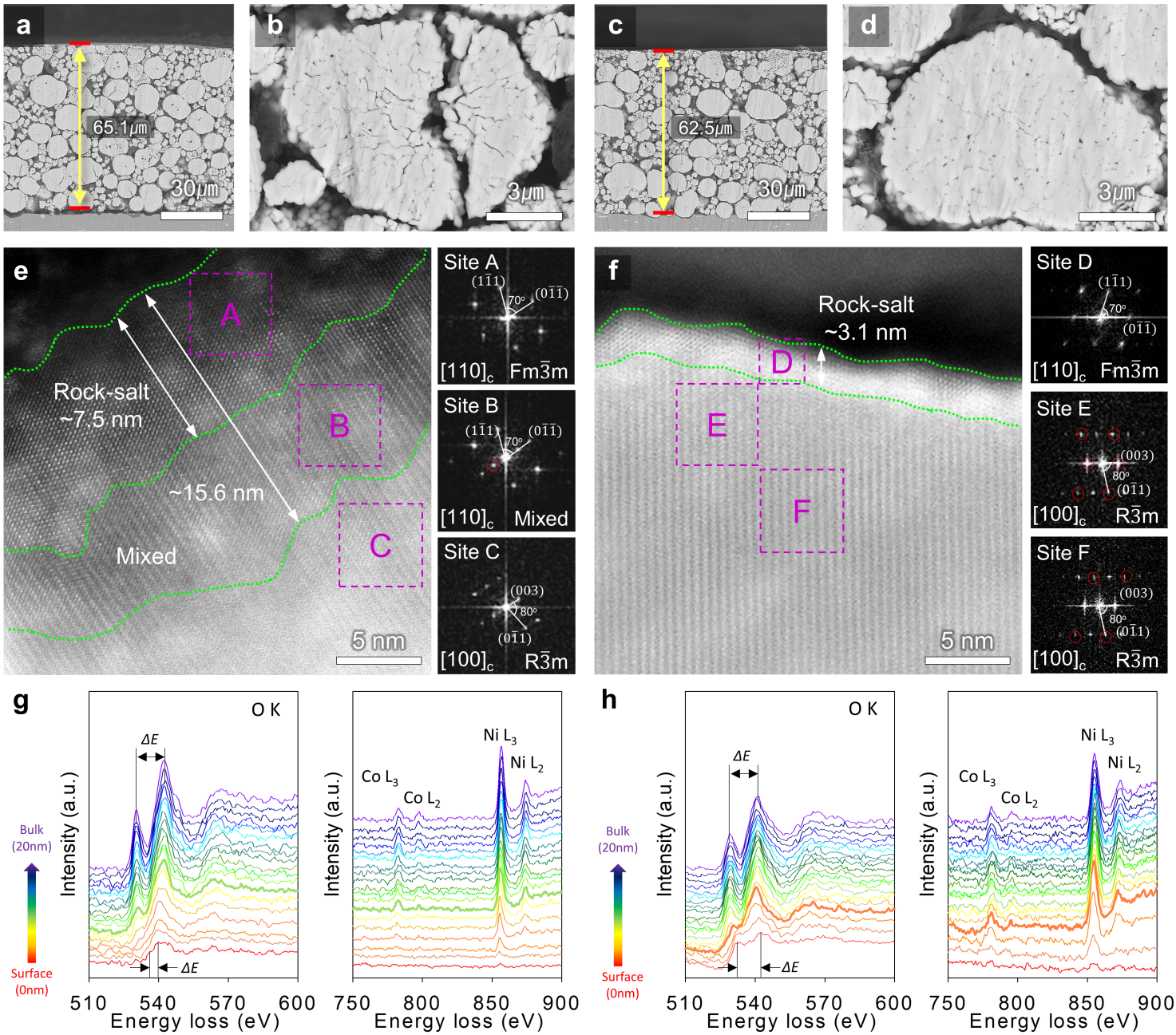

Figure 9

Characterization of NCM811 cathodes recovered from full cells after 100 cycles at 45 °C. Cross-sectional morphologies of the corresponding pristine NCM811 cathode and cathodes from full cells with **a, b,** VC electrolyte or **c, d,** VC+APFS electrolyte. STEM images with their FFT patterns of NCM811 cathodes with **e,** the VC or **f,** VC+APFS electrolyte. EELS plots in the range of 0–20 nm of cycled NCM811 cathodes for the O K-, Co L-, Ni L_3 and L_2-edge spectra with **g,** the VC or **h,** VC+APFS electrolyte.

Supplementary Files

This is a list of supplementary files associated with this preprint. Click to download.

- SupplementaryInformation.docx